Revision 1

Pressure-induced phase transitions in Ni-bearing ferrosilite (Ni-$En_{31}Fs_{65}$)

Jingui Xu[1, 2*], Dawei Fan[1*], Dongzhou Zhang[2], Bo Li[3], Wenge Zhou[1], Przemyslaw Dera[2]

[1]Key Laboratory for High-Temperature and High-Pressure Study of the Earth's Interior, Institute of Geochemistry, Chinese Academy of Sciences, Guiyang, Guizhou 550081, China.

[2]Hawai'i Institute of Geophysics and Planetology, School of Ocean and Earth Science and Technology, University of Hawai'i at Manoa, Honolulu, Hawaii 96822, United States.

[3]Research Institute of Petroleum Exploration & Development-Northwest (NWGI), PetroChina, Lanzhou 730060, Gansu, China.

*Correspondence to: J. Xu and D. Fan

jgxu107@gmail.com; fandawei@vip.gyig.ac.cn

Abstract

Orthopyroxene is an abundant mineral in subducting slabs. Studies on its phase transitions at high pressure are important to understand the mineralogy of subducting slabs in the deep Earth. Synchrotron-based single-crystal X-ray diffraction experiments were conducted on a synthetic Ni-bearing ferrosilite (Ni-$En_{31}Fs_{65}$) at high pressures up to 33.8 GPa. Three phase transitions were observed at 12.1(6) GPa, 15.6(6) GPa, and 31.3(25) GPa, respectively. The first two phase transitions in Ni-$En_{31}Fs_{65}$ resemble the previously described phase transitions in Ni-free Fe-rich orthopyroxenes, i.e., the initial α-opx (*Pbca*) transforms into the β-opx ($P2_1/c$), then the latter transforms into the γ-opx (*Pbca*). This indicates that the incorporation of a few mol. % $NiSiO_3$ does not influence the phase transition path of Fe-rich orthopyroxene. After the third phase transition, the structure ($P2_1ca$) of Ni-$En_{31}Fs_{65}$ resembles the previously reported β-popx observed in En_{90} at high pressure, although the onset pressure of the phase transition in Ni-$En_{31}Fs_{65}$ is ~7 GPa lower than that in En_{90}. β-popx has a post-pyroxene structure that contains five and six coordinated Si cations. The results of this study indicate that the post-pyroxene structure is β-popx ($P2_1ca$) for either Fe-poor or Fe-rich orthopyroxenes, although the phase transition path before the pyroxene → post-pyroxene is compositionally dependent. Additionally, unlike the second and third transitions, whose onset pressures are monotonously decreased by increasing Fe content, the Fe effect on shifting the first transition is much more significant for orthopyrxoenes within En < 50 mol. % than that within En > 50 mol. %.

Introduction

Orthopyroxene is a major rock-forming mineral in the subducting oceanic slabs. A typical subducting slab is composed of three layers, with the basaltic crust layer atop, and the residual harzburgite and lherzolite at the middle and bottom, respectively (Ringwood 1982). Harzburgite and lherzolite commonly contain more than 20 vol. % orthopyroxene (Bodinier and Godard 2007). It has been proposed that pyroxene minerals could survive as metastable phases in cold subducting slabs as the low-temperature conditions largely inhibit the pyroxene-majorite transition (Nishi et al. 2013; Van Mierlo et al. 2013). Therefore, investigating the phase transitions of orthopyroxene at high pressures and high temperatures is important to understand the mineralogy of subducting slabs.

In recent years, room-temperature high-pressure single-crystal X-ray diffraction (SCXRD) has revealed several high-pressure phases of orthopyroxene. The initial orthopyroxene (α-opx, *Pbca* space group) transforms into a monoclinic structure (β-opx, $P2_1/c$) at pressures ranging from 6 GPa to 16 GPa depending on the contents of Fe, Al and Ca (e.g., Lin et al. 2005; Zhang et al. 2012; Dera et al. 2013a; Zhang et al. 2013a; Zhang et al. 2013b; Finkelstein et al. 2015; Xu et al. 2020; Li et al. 2022). With increasing pressure, β-opx transforms into α-popx ($P2_1ca$; Finkelstein et al. (2015) when the molar percentage (M; mol. %) of enstatite (En, $MgSiO_3$) of the sample is higher than ~80 mol. %, otherwise it transforms into γ-opx (*Pbca*; Dera et al. 2013a). The onset pressure (12-31 GPa) of the β-opx → γ-opx transition is also depending on the contents of Fe, Al, and Ca (Xu et al. 2020; Xu et al. 2022). After the β-opx → γ-opx transition, no further phase transitions have been observed; in comparison, α-popx → β-popx ($P2_1ca$, post-pyroxene structure; Finkelstein et al. (2015) transition in $En_{90}Fs_{10}$ (Fs is ferrosilite, $FeSiO_3$) has been observed at ~40 GPa. It should be noted that the high-pressure SCXRD measurement (Xu et al. 2018) up to 34 GPa did not observe phase transition in end-member enstatite (En_{100}) after the α-opx → β-opx transition but high-pressure Raman spectroscopy experiment (Serghiou et al. 2000) revealed a new phase (at ~40 GPa) whose structure resembles that of the β-popx after the α-opx → β-opx transition. High-pressure and high-temperature SCXRD and Raman spectroscopy studies revealed that the α-opx → β-opx → γ-opx transitions could occur for orthopyroxenes under the pressure-temperature conditions of the cold slab center within the transition zone (Zhang et al. 2014; Xu et al. 2022).

Nonetheless, the compositional effects on the high-pressure phase transition of orthopyroxene have not yet been well constrained. On the one hand, β-popx is observed as the high-pressure phase for En_{90} after the β-opx → α-popx transition (Finkelstein et al. (2015). But it is still unclear whether β-popx is also the high-pressure phase of orthopyroxenes that are more Fe-rich than En_{90} after the β-opx → γ-opx transition. On the other hand, Xu et al. (2022) found that, for the En-Fs solid solutions, varying Fe content has little effect on the pressure of the α-opx → β-opx ($P_{\alpha\text{-}\beta}$) within M_{En} = 44 - 100, and suggested that the effect of varying Fe on $P_{\alpha\text{-}\beta}$ is more significant within M_{En} = 0 - 44, which needs to be verified. Thus, studies on the high-pressure phase transitions of Fe-rich orthopyroxenes are needed to address these concerns.

Other than Fe, Al, and Ca, Ni commonly occurs in natural orthopyroxene and the NiO content in orthopyroxene can be as high as ~1 wt. % in Ni-enriched mantle peridotite (Ishimaru and Arai 2008). Thus, experimental studies on Ni-bearing orthopyroxene could provide a more comprehensive understanding of the phase transitions of orthopyroxene group. Our recent study has reported that Ni-bearing enstatite ($Mg_{0.95}Ni_{0.05}SiO_3$) transforms from the initial α-opx into the β-opx at 13.5 GPa but with increasing pressure, the β-opx does not transform into the γ-opx or the α-popx, instead, it transforms into a new high-pressure phase (β-opxII, $P2_1/c$ space group) at 29.8 GPa (Xu et al. 2018), indicating that the incorporation of a few mol. % $NiSiO_3$ could change the phase transitions of orthopyroxene at high pressures. However, it remains unknown whether the incorporation of a few mol. % $NiSiO_3$ would influence the phase transitions of Fe-rich orthopyroxenes at high pressures. The answer to this is important for us when we model the metastable phases of Ni-, Fe-bearing orthopyroxene in the deep earth, which demands further studies on the high-pressure phase transitions of Ni-, Fe-bearing orthopyroxene.

Therefore, in this study, we performed high-pressure SCXRD experiments on a synthetic Ni-bearing ferrosilite to constrain the compositional (Ni and Fe) effects on the phase transitions of orthopyroxene.

Experiments

We synthesized the Ni-bearing ferrosilite from a mixture of high-purity SiO_2, MgO, Fe_2O_3, Fe, and NiO, using a multi-anvil press apparatus at the Institute of Geochemistry, Chinese Academy of Sciences. The sample synthesis was conducted at 1000 °C and 3 GPa for 24 hours, and the detailed description can be seen in the authors' previous study (Xu et al. 2018). The obtained crystals from the quenched samples were between 40-100 μm in size. Electron microprobe analyses (EMPA) were carried out using a JXA 8230, operating at an acceleration voltage of 15 kV and a beam current of 20 nA, and the focused beam was ~5 μm. The chemical formula was estimated as $Mg_{0.31}Fe_{0.65}Ni_{0.04}SiO_3$ (Ni-$En_{31}Fs_{65}$, hereafter).

We selected a crystal with a size ca. 40 × 20 × 10 μm^3 and loaded it into a short-symmetric diamond anvil cell (DAC) for the ambient and high-pressure SCXRD experiments. The DAC was equipped with two type-I diamonds with 300 μm culet size and two Boehler-Almax-type WC seats, allowing a ±32 ° opening angle. A rhenium plate with an initial thickness of 250 μm was indented to ~50 μm to serve as the gasket, and a laser-drilled hole with 180 μm in diameter in the indented area was the sample chamber. The selected crystal, a small ruby sphere, and a gold foil were loaded into the sample chamber (Figure 1) before loading neon as the pressure medium using the gas loading system at GSECARS, Advanced Photon Source (APS; Rivers et al. 2008). The gold foil (Fei et al. 2007) was used as the pressure marker in the processes of high-pressure experiments.

The SCXRD experiments were carried out with a six-circle diffractometer at the experimental station 13-BM-C of APS, Argonne National Laboratory. The incident X-ray was monochromated to a wavelength of 0.434 Å with a focused beam size of 12 ×

18 μm^2. A MAR165 CCD was used to acquire the diffraction image, and the tilting and rotation of the detector and the sample-to-detector distance were calibrated using LaB_6 powder as the diffraction standard (Zhang et al. 2017). We collected diffraction data at 27 different pressures from room pressure to 33.8 GPa. We noted that as the sample chamber shrank too much, the highest experimental pressure was 33.8 GPa. As shown in Figure 1(d) the Re peaks occurred when we collected sample data at 33.8 GPa, indicating that high-quality SCXRD data cannot be ensured at higher pressures. At each pressure, the φ-rotation scan was with a step size of 1 ° and an exposure time of 1 s/°, and the rotation range was the same as the DAC opening angle. Besides, we collected increased diffraction peaks with multiple detector positions (Xu et al. 2017a) at 10 of the 27 pressures for full structure determination.

The diffraction images were processed using the GSE_ADA/RSV software package (Dera et al. 2013b) to extract the unit-cell information and peak intensities. The refined unit-cell parameters are shown in Table S1. We used SHELXL (Sheldrick 2008) software via Olex2 (Dolomanov et al. 2009) user interface to refine the crystal structure at different pressures, and the VESTA software (Momma and Izumi 2011) was used to calculate polyhedral parameters. We used the orthopyroxene structure from the previous study (Xu et al. 2018) as the starting model. According to the chemical formula of orthopyroxene ($M02M01T_2O_6$), the M01 and M02 site was set to be fully occupied by Mg and Fe, while the T site was set to be filled with Si. We did not consider Ni in the refinement as it has a similar electron number to Fe and its insignificant content compared to Mg and Fe. We used the chemical data from the EMPA to constrain the overall contents of Fe and Mg during the structural refinement. Atoms residing at the same site were constrained to share the same atomic displacement parameters (ADPs) and the same fractional coordinates. Isotropic ADPs were used for all atoms. The crystallographic information files (CIF) are available in the supporting material. The structural refinement details, atomic coordinates, occupancies, bond lengths, and polyhedral parameters are summarized in Tables S2-S7.

Results

The Ni-$En_{31}Fs_{65}$ underwent three phase transitions with increasing pressure up to 33.8 GPa. As shown by the diffraction images in Figure 1, diffraction peak changes occurred at 12.7 GPa, 16.2 GPa, and 33.8 GPa, indicating structure changes. From room pressure to 11.5 GPa, the diffraction peaks were perfectly indexed with the initial α-opx and the unit-cell parameters *a*, *b,* and *c* decreased with increasing pressure (Figure 2 and Table S1). At 12.7 GPa, diffraction peak indexing led to a monoclinic unit cell similar to that of the β-opx phase reported in previous studies (Dera et al. 2013a; Finkelstein et al. 2015), and analysis of the symmetry also obtained a $P2_1/c$ space group. The β-opx survived up to 15.0 GPa, and its structure was refined using the previously reported structure (Dera et al. 2013a) as the starting model (Table S3(b)). At 16.2 GPa, diffraction peak indexing and structural analysis yielded an orthorhombic unit cell with a *Pbca* space group (Figure 2 and Table S1), and the structure refinement indicated that this phase is the previously reported γ-opx (Table S3(c); Dera et al. (2013a)). The γ-opx persisted up to 28.8 GPa with its unit-cell parameters *a*, *b,* and *c* decreasing with pressure (Figure 2). At 33.8 GPa, diffraction peak indexing also yielded an orthorhombic unit cell, but the structural analysis indicated a $P2_1ca$ space group. Its structure was solved and refined with the $P2_1ca$ space group (Table S3(d)), indicating that this structure is the same as the β-popx (Finkelstein et al. 2015).

The unit-cell parameters varied differently through the phase transitions. As shown in Figure 2, as α-opx transforms to β-opx, the *a* and *b* increased by 0.3% and 0.7%, respectively; by contrast, the *c* decreased by 2.3%. In the second phase transition, the *a* and *b* increased by 0.2% and 0.3%, respectively, while the *c* decreased by 2.3%. In the γ-opx → β-popx transition, the *a* increased by 0.8% while the *b* and *c* decreased by 6.7% and 2.5%, respectively. The volume drops were 1.4%, 1.7%, and 6.3% for the α-opx → β-opx, β-opx → γ-opx, and γ-opx → β-popx transitions, respectively.

The crystal structure of the α-opx has four crystallographically distinct polyhedra, $M01O_6$ and $M02O_6$ octahedra and $Si01O_4$ and $Si02O_4$ tetrahedra. $M01O_6$ and $M02O_6$ octahedra connect each other to form layers parallel to the *bc* plane. $Si01O_4$ and $Si02O_4$ tetrahedra separately form chains extending in the *c* direction. $Si01O_4$ and $Si02O_4$ chains alternately separate the layers formed by $M01O_6$ and $M02O_6$ octahedra. Within the stable region of the α-opx, the bond lengths of the $M01O_6$ octahedron decreased by 2.3-4.4% as the pressure increased from room pressure to 11.5 GPa (Figure 3(a)); however, the bond lengths of the $M02O_6$ octahedron varied differently with increasing pressure, as shown in Figure 3(a), the bond length of M02-O02 increased by 3.0% while the other bond lengths decreased by 1.6-11.0%. In comparison, as the pressure increases from room pressure to 11.5 GPa, the bond lengths of the $Si01O_4$ and $Si02O_4$ tetrahedra decreased by 0.2-1.2% and 0.1-3.1% (Figure 4(a)), respectively. The volumes of the $M01O_6$ and $M02O_6$ octahedra decreased by 10.0% and 11.0% (Figure 5(a)) over the pressure range of the α-opx, respectively, and the volumes of the $Si01O_4$ and $Si02O_4$ tetrahedra decreased by 1.0% and 3.5% (Figure 5(b)), respectively.

The distortion index, quadratic elongation, and bond angle variance parameters (Robinson et al. 1971) were used to evaluate the nonideality of the coordination polyhedra. As shown in Figure 6, at room pressure, the distortion index, quadratic elongation, and bond angle variance of the $M02O_6$ octahedron are larger than the $M01O_6$, indicating that the $M01O_6$ octahedron is closer to the ideal octahedron in comparison to the $M02O_6$ octahedron. As the pressure increased from room pressure to 11.5 GPa, the distortion index of the $M02O_6$ decreased by 41.4% (Figure 6) but the quadratic elongation and bond angle variance only decreased by 0.9% and 0.4%, respectively, in comparison, the distortion index, quadratic elongation, and angular variance of the $M01O_6$ octahedron decreased by 1.9%, 0.1%, and 7.6%, respectively. The quadratic elongation of the $Si01O_4$ and $Si02O_4$ tetrahedra only decreased by 0.1% as the pressure increased to 11.5 GPa (Figure 7); however, the distortion index of the $Si01O_4$ and $Si02O_4$ tetrahedra decreased by 23.7% and 15.7%, respectively, and the bond angle variance of these two tetrahedra decreased by 17.7% and 21.5%, respectively.

As the α-opx transformed into the β-opx, due to the symmetry change ($Pbca \rightarrow P2_1/c$), the M01 and M02 were split into two crystallographically distinct sites (M01a/M01b and M02a/M02b). As shown in Figure 5(a), at 14.2 GPa, the volumes of the M02aO_6 and M02bO_6 octahedra are larger than the volumes of the M01aO_6 and the M01bO_6 octahedra. Likewise, Si01 and Si02 were split into two Si01a/Si01b and Si02a/Si02b, respectively. The volumes of the Si01bO_4 and Si02bO_4 tetrahedra are larger than the volumes of the Si01aO_4 and Si01bO_4 tetrahedra (Figure 5(b)). Nevertheless, after the β-opx transformed into the γ-opx, only four crystallographically distinct cationic sites exist in the structure, two octahedrally coordinated (M01 and M02) and two tetrahedrally coordinated (Si01 and Si02) sites. Through the α-opx → β-opx → γ-opx phase transitions, the distortion index, quadratic elongation, and bond angle variance of the M01O_6 octahedron did not change significantly (Figure 6) but the quadratic elongation and bond angle variance of the M02O_6 octahedron decreased by 3.9% and 77.3% (Figure 6(b-c)), respectively, when pressure increased from 11.5 to 17.3 GPa.

At 33.8 GPa, as the γ-opx transformed into the β-popx, the octahedrally coordinated M01 and M02 split into M01a/M01b and M02a/M02b again, and the tetrahedrally coordinated Si01 and Si02 also split into Si01a/Si01b and Si02a/Si02b, due to the lowering of the symmetry from *Pbca* to $P2_1ca$ (Figures 3-7). The coordination numbers of Si cations changed during this phase transition. As shown in Figure 4 and Tables S6-S7, while the Si01a remained tetrahedrally coordinated, the other three Si cations increased in coordination number (Finkelstein et al. 2015). The Si01b cation was penta-coordinated to form a highly distorted trigonal bipyramid (Figure 7(a)) with a distinctly longer Si01b-O (Si01b-O03 = 2.09(7) Å; Table S7) bond than the other four (1.47(6)-1.90(7) Å). In comparison, Si02a and Si02b were octahedrally coordinated in the β-popx (Figure 4(c)), and the Si-O bond lengths in the Si02aO_6 and Si02bO_6 octahedra were 1.64(7)-1.88(7) Å and 1.60(8)-1.89(6) Å (Table S7), respectively.

The pressure-volume data of the α-opx and γ-opx were separately fitted to a Birch-Murnaghan equation of state (BMEoS; Birch (1947)) using the Eosfit7c software package (Angel et al. 2014) to obtain their EoS parameters, and we did not fit the data of β-opx and β-popx to an EoS because of their limited data points. A third-order BMEoS fit to the data of the α-opx obtained the zero-pressure volume (V_{T0}), zero-pressure bulk modulus (K_{T0}) and its pressure derivative (K'_{T0}), V_{T0} = 858.4(3) Å^3, K_{T0} = 91(5) GPa, and K'_{T0} = 8.7(17); while V_{T0} = 858.4(3) Å^3 and K_{T0} = 93(1) GPa were obtained when K'_{T0} was fixed at 8.0 (the K'_{T0} for En_{100}; (Angel and Jackson 2002; Xu et al. 2018)). We also obtained V_{T0} = 828.2(76) Å^3 and K_{T0} = 134(12) GPa for the γ-opx by fitting the pressure-volume data to the second-order BMEoS with fixed K'_{T0} = 4.

Discussion

Xu et al. (2018) observed after the α-opx → β-opx phase transition the β-opx → β-opxII phase transition in a Ni-bearing Fe-free enstatite. However, this study revealed that the Ni-$En_{31}Fs_{65}$ underwent the α-opx → β-opx → γ-opx → β-popx phase transitions as the pressure increased from room pressure to 33.8 GPa, indicating that the β-opx → β-opxII phase transition does not occur for the Ni-$En_{31}Fs_{65}$. In addition, the observation of the β-opx → γ-opx phase transition in this study indicates that the phase transition of Ni-bearing Fe-rich orthopyroxene resembles Ni-free Fe-rich orthopyroxene (Figure 8). The α-opx → β-opx → γ-opx phase transitions mainly involve the SiO_4 tetrahedral rotation as the structural change as suggested by previous studies (e.g., Dera et al. 2013a), as a result, the *c* (the extending direction of the tetrahedra chains) is decreased much more significantly in comparison to the *a* and *b* (Figure 2) during these two phase transitions.

Previous studies reported the occurrence of the β-popx as a high-pressure phase in $En_{90}Fs_{10}$ (Finkelstein et al. 2015) and En_{100} (Serghiou et al. 2000) but not yet in more Fe-rich orthopyroxenes. $En_{90}Fs_{10}$ transforms from the α-popx to the β-popx after the α-opx → β-opx → α-popx phase transitions while En_{100} transforms into the β-popx from the β-opx (Figure 8). The results of this study indicate that the β-popx also occurs in Fe-rich orthopyroxenes at high pressure, although the transition path could be different from those of $En_{90}Fs_{10}$ and En_{100} (Figure 8). Unlike the α-opx → β-opx → γ-opx phase transitions, the γ-opx → β-popx phase transition is characterized by the coordination number increase in the Si cations. While half of the Si01 cations (Si01a) are still tetrahedrally coordinated in the β-popx as they are in the γ-opx, the other half (Si01b) increase from four to five in coordination number as the γ-opx transforms into β-popx. In comparison, all the Si02 (Si02a and Si02b) cations increase their coordination numbers from four in the γ-opx to six in the β-popx (Table S7). The increase in the coordination number of Si resulted in a much larger volume drop of γ-opx → β-popx phase transition (6.3%) in comparison to the α-opx → β-opx (1.4%) and the β-opx → γ-opx (1.7%) phase transition.

The pressures of the phase transitions (P_{tr}) in the Ni-$En_{31}Fs_{65}$ follow the P_{tr}-composition relationship in the En-Fs solutions and the data do not show offset due to the presence of Ni. In addition, while the P_{tr} of the second (β-opx → γ-opx/α-popx) and third (γ-opx/α-popx/β-opx → β-popx) transition are monotonously decreased by increasing Fe, our data confirm that there exists a offset around $M_{En} = 50$ for the first phase transition (α-opx → β-opx), and the Fe-effect on shifting the P_{tr} (α-opx → β-opx) is much more significant for orthopyroxenes within $M_{En} < 50$ than that within $M_{En} > 50$ (Figure 8). Therefore, we refined the metastable phase boundaries of orthopyroxenes by including the Ni-$En_{31}Fs_{65}$ data in the fitting (Table S8 and Figure 8), following the track of Xu et al., (2022). For the first phase transition, since there exists an offset around $M_{En} = 50$, we only fit $M_{En} < 50$ data points ($En_{44}Fs_{56}$, Ni-$En_{31}Fs_{65}$, $En_{14}Fs_{82}$, and Fs_{100}), and the result is $P_{tr} = 8.9(9) + 0.09(3)M_{En}$, $R^2 = 0.86$; for the second phase transition, a linear fitting of 7 data points ($En_{90}Fs_{10}$, $En_{70}Fs_{30}$, $En_{55}Fs_{45}$, $En_{44}Fs_{56}$, Ni-$En_{31}Fs_{65}$, $En_{14}Fs_{82}$, and Fs_{100}) yield $P_{tr} = 11.4(9) + 0.18(2)M_{En}$, $R^2 = 0.95$; for the third phase transition, 3 data points (Ni-$En_{31}Fs_{65}$, En_{90}, and En_{100}) are used for a linear fitting, and the resulted formula is $P_{tr} = 28.0(12) + 0.11(1)M_{En}$, $R^2 = 0.98$.

Implications

In cold subducting slabs, the temperature in the slab could be several hundred K lower than that of the normal mantle (Syracuse et al. 2010; King et al. 2015). Under such low-temperature conditions, pyroxene could survive as metastable phases in the cold subducting slab to the transition zone, since the pyroxene → majorite transition is largely inhibited in geological time scales under the low-temperature conditions in the slab (Nishi et al. 2013; Van Mierlo et al. 2013). It has been proposed that metastable pyroxene transforms into akimotoite (Hogrefe et al. 1994) in the transition zone, which plays an important role in subducting slab dynamics. However, in situ high-pressure XRD experiments (Pakhomova et al. 2017; Lazarz et al. 2019) suggest that metastable pyroxene likely does not transform into akimotoite directly. On the contrary, high-pressure SCXRD experiments have revealed the pyroxene → post-pyroxene (like the γ-opx → β-popx phase transition in this study) transition in several pyroxene minerals. The post-pyroxene means that the structure remains pyroxene-like M01 and M02 sites, but five and six coordination exist in its Si cations (Finkelstein et al. 2015).

Natural pyroxene minerals are divided in terms of their crystal structures (orthorhombic and monoclinic) into orthopyroxene and clinopyroxene (Nesse 2000). For the subducting slab, the most important end members of orthopyroxene are En_{100} and Fs_{100}. Diopside (Di, $CaMgSi_2O_6$) and hedenbergite (Hd, $CaFeSi_2O_6$) are the most important end-member Ca-clinopyroxenes; jadeite (Jd, $NaAlSi_2O_6$) and aegirine (Aeg, $NaFe^{3+}Si_2O_6$) are the most important end-member Na-clinopyroxenes. The common Ca- and Na-free end-member clinopyroxenes are clinoenstatite (Cen, $MgSiO_3$) and clinoferrosilite (Cfs, $FeSiO_3$).

The pyroxene → post-pyroxene transition has been revealed at room temperature and high pressure in both orthopyroxene and clinopyroxene (Figure 9). The post-pyroxene structure of orthopyroxene has been obtained in En_{100} (Serghiou et al. 2000), En_{90} (Finkelstein et al. 2015), and Ni-$En_{31}Fs_{65}$ (This study) at 39.0 GPa, 38.6 GPa, and 31.3 GPa, respectively. In comparison, the pyroxene → post-pyroxene transition occurs at 43.2 GPa in clinoenstatite (Lazarz et al. 2019) and 33.0 GPa in clinoferrosilite (Pakhomova et al. 2017). The Ca-clinopyroxenes transform from the initial pyroxene structure into their post-pyroxene structure at distinctly higher pressures than orthopyroxenes. As shown in Figure 9, the post-pyroxene structure occurs in Di_{75} (Hu et al. 2017) and Di_{97} (Plonka et al. 2012) at 51.8 GPa and 49.4 GPa, respectively. Synchrotron-based nuclear forward scattering experiment observed a phase transition in Hd_{100} between 53 and 68 GPa (Zhang et al. 1999) which might be related to the pyroxene → post-pyroxene transition. On the contrary, the pyroxene → post-pyroxene transition has not yet been reported in Na-clinopyroxene. SCXRD up to 30.4 GPa did not observe any phase transition in Jd_{100} (Posner et al. 2014); likewise, no phase transition occurs in a solid solution $Di_{51}Jd_{49}$ up to 47 GPa (Zhang et al. 2016). The pyroxene → post-pyroxene transition was also not obtained in Aeg_{100} up to 60 GPa (Xu et al. 2017b). Since the pyroxene → post-pyroxene transition seems to occur at lower pressures in Fe-rich pyroxenes than in Fe-poor pyroxenes (Figure 9), this phase transition might occur in Na-clinopyroxenes at pressures higher than 60 GPa.

Therefore, the pyroxene → post-pyroxene transition seems unlikely to occur in the Earth's transition zone (440-660 km) according to the results of in-situ room-temperature high-pressure experiments. As shown in Figure 9, the pyroxene → post-pyroxene transition occurs in Ni-$En_{31}Fs_{65}$ at 31.3 GPa (corresponding to a depth of ~850 km) which has been the lowest pressure thus far that enables this phase transition. Increasing temperature likely enables this phase transition to occur at lower pressures than at room temperature (Hu et al. 2017). However, single-crystal XRD studies on pyroxene minerals at simultaneously high pressure and high temperature up to the pressures corresponding to the transition zone depths are still limited. High-pressure-temperature single-crystal XRD up to ~25 GPa and 800 K did not observe the pyroxene → post-pyroxene transition in orthopyroxenes with various compositions (e.g., Xu et al. 2020). The post-pyroxene was also not observed in natural augite (Di_{74}; Xu et al. 2017a) and in a natural omphacite ($Di_{57}Jd_{43}$; Xu et al. 2019) at high pressure-temperature up to ~25 GPa and 700 K. Geophysical modeling estimated the current temperatures in cold stagnant slab interior in the transition zone ranging from ~800 K to ~1200 K depending on the location of the slab (King et al. 2015). Therefore, more high-pressure-temperature investigations at temperatures up to 1200 K are needed on the pyroxene → post-pyroxene transition in different kinds of pyroxene for a better understanding of its role in the subducting slab dynamics.

Acknowledgments

We acknowledge Sergey N. Tkachev for the gas loading assistance. We thank two anonymous reviewers for their helpful comments, which helped to improve the quality of this manuscript. We thank O. Tschauner for handling this manuscript. This work was supported by the "Hundred Talents Program of the Chinese Academy of Sciences", the National Natural Science Foundation of China (42172048) , and Guizhou Provincial Outstanding Youth Science and Technology Talent Project. The diffraction experiments were performed at GeoSoilEnviroCARS, Sector13-BM-C, Partnership for Extreme Crystallography program (PX^2), Advanced Photon Source (APS), and Argonne National Laboratory. GeoSoilEnviroCARS is supported by the National Science Foundation—Earth Sciences (EAR-1634415) and the Department of Energy—Geosciences (DE-FG02-94ER14466). PX^2 program is supported by COMPRES under NSF Cooperative Agreement EAR-1661511. The use of the COMPRES-GSECARS gas loading system was supported by COMPRES under NSF Cooperative Agreement EAR-1661511 and by GSECARS. Use of the APS was supported by the U.S. Department of Energy, Office of Science, Office of Basic Energy Sciences, under Contract No. DE-AC02-06CH11357.

References

Angel, R.J., Gonzalez-Platas, J., and Alvaro, M. (2014) EosFit7c and a Fortran module (library) for equation of state calculations. Zeitschrift für Kristallographie - Crystalline Materials, 229(5), 405-419.

Angel, R.J., and Jackson, J.M. (2002) Elasticity and equation of state of orthoenstatite, $MgSiO_3$. American Mineralogist, 87(4), 558-561.

Birch, F. (1947) Finite elastic strain of cubic crystals. Physical Review, 71(11), 809-824.

Bodinier, J.L., and Godard, M. (2007) Orogenic, Ophiolitic, and Abyssal Peridotites. In H.D. Holland, and K.K. Turekian, Eds. Treatise on Geochemistry, 2, p. 1-73. Pergamon, Oxford.

Dera, P., Finkelstein, G.J., Duffy, T.S., Downs, R.T., Meng, Y., Prakapenka, V., and Tkachev, S. (2013a) Metastable high-pressure transformations of orthoferrosilite Fs_{82}. Physics of the Earth and Planetary Interiors, 221, 15-21.

Dera, P., Zhuravlev, K., Prakapenka, V., Rivers, M.L., Finkelstein, G.J., Grubor-Urosevic, O., Tschauner, O., Clark, S.M., and Downs, R.T. (2013b) High pressure single-crystal micro X-ray diffraction analysis with GSE_ADA/RSV software. High Pressure Research, 33(3), 466-484.

Dolomanov, O.V., Bourhis, L.J., Gildea, R.J., Howard, J.A., and Puschmann, H. (2009) OLEX2: a complete structure solution, refinement and analysis program. Journal of Applied Crystallography, 42(2), 339-341.

Fei, Y., Ricolleau, A., Frank, M., Mibe, K., Shen, G., and Prakapenka, V. (2007) Toward an internally consistent pressure scale. Proceedings of the National Academy of Sciences of the United States of America, 104(22), 9182-9186.

Finkelstein, G.J., Dera, P.K., and Duffy, T.S. (2015) Phase transitions in orthopyroxene (En_{90}) to 49 GPa from single-crystal X-ray diffraction. Physics of the Earth and Planetary Interiors, 244, 78-86.

Hogrefe, A., Rubie, D., Sharp, T., and Seifert, F. (1994) Metastability of enstatite in deep subducting lithosphere. Nature, 372(6504), 351-353.

Hu, Y., Kiefer, B., Bina, C.R., Zhang, D., and Dera, P.K. (2017) High-Pressure γ-$CaMgSi_2O_6$: Does Penta-Coordinated Silicon Exist in the Earth's Mantle? Geophysical Research Letters, 44(22), 11,340-11,348.

Hugh-Jones, D., Chopelas, A., and Augel, R. (1997) Tetrahedral compression in (Mg, Fe)SiO_3 orthopyroxenes. Physics and Chemistry of Minerals, 24(4), 301-310.

Hugh-Jones, D.A., and Angel, R.J. (1994) A compressional study of $MgSiO_3$ orthoenstatite up to 8.5 GPa. American Mineralogist, 79(5-6), 405-410.

Ishimaru, S., and Arai, S. (2008) Nickel enrichment in mantle olivine beneath a volcanic front. Contributions to Mineralogy and Petrology, 156(1), 119-131.

King, S.D., Frost, D.J., and Rubie, D.C. (2015) Why cold slabs stagnate in the transition zone. Geology, 43(3), 231-234.

Lazarz, J.D., Dera, P., Hu, Y., Meng, Y., Bina, C.R., and Jacobsen, S.D. (2019) High-pressure phase transitions of clinoenstatite. American Mineralogist, 104(6), 897–904.

Li, L., Sun, N., Shi, W., Mao, Z., Yu, Y., Zhang, Y., and Lin, J.F. (2022) Elastic Anomalies Across the α-β Phase Transition in Orthopyroxene: Implication for the Metastable Wedge in the Cold Subduction Slab. Geophysical Research Letters, 49(16).

Lin, C.-M., Chao, J., and Lin, C.-C. (2005) Metastable phase transition of orthoenstatite ($MgSiO_3$) under high pressure. Solid state sciences, 7(3), 293-297.

Momma, K., and Izumi, F. (2011) VESTA 3 for three-dimensional visualization of crystal, volumetric and morphology data. Journal of Applied Crystallography, 44(6), 1272-1276.

Nesse, W.D. (2000) Introduction to mineralogy. Oxford University Press New York.

Nishi, M., Kubo, T., Ohfuji, H., Kato, T., Nishihara, Y., and Irifune, T. (2013) Slow Si-Al interdiffusion in garnet and stagnation of subducting slabs. Earth and Planetary Science Letters, 361, 44-49.

Pakhomova, A., Ismailova, L., Bykova, E., Bykov, M., Boffa Ballaran, T., and Dubrovinsky, L. (2017) A new high-pressure phase transition in clinoferrosilite: In situ single-crystal X-ray diffraction study. American Mineralogist, 102(3), 666-673.

Periotto, B., Balić-Žunić, T., Nestola, F., Katerinopoulou, A., and Angel, R.J. (2012) Re-investigation of the crystal structure of enstatite under high-pressure conditions. American Mineralogist, 97(10), 1741-1748.

Plonka, A.M., Dera, P., Irmen, P., Rivers, M.L., Ehm, L., and Parise, J.B. (2012) β-diopside, a new ultrahigh-pressure polymorph of $CaMgSi_2O_6$with six-coordinated silicon. Geophysical Research Letters, 39(24).

Posner, E.S., Dera, P., Downs, R.T., Lazarz, J.D., and Irmen, P. (2014) High-pressure single-crystal X-ray diffraction study of jadeite and kosmochlor. Physics and Chemistry of Minerals, 41(9), 695-

707.

Ringwood, A.E. (1982) Phase transformations and differentiation in subducted lithosphere: implications for mantle dynamics, basalt petrogenesis, and crustal evolution. The Journal of Geology, 90, 611-643.

Rivers, M., Prakapenka, V.B., Kubo, A., Pullins, C., Holl, C.M., and Jacobsen, S.D. (2008) The COMPRES/GSECARS gas-loading system for diamond anvil cells at the Advanced Photon Source. High Pressure Research, 28(3), 273-292.

Robinson, K., Gibbs, G., and Ribbe, P. (1971) Quadratic elongation: a quantitative measure of distortion in coordination polyhedra. Science, 172(3983), 567-570.

Serghiou, G., Boehler, R., and Chopelas, A. (2000) Reversible coordination changes in crystalline silicates at high pressure and ambient temperature. Journal of Physics: Condensed Matter, 12(6), 849.

Sheldrick, G.M. (2008) A short history of SHELX. Acta Crystallogr A, 64(Pt 1), 112-22.

Syracuse, E.M., van Keken, P.E., and Abers, G.A. (2010) The global range of subduction zone thermal models. Physics of the Earth and Planetary Interiors, 183(1), 73-90.

Van Mierlo, W., Langenhorst, F., Frost, D., and Rubie, D. (2013) Stagnation of subducting slabs in the transition zone due to slow diffusion in majoritic garnet. Nature Geoscience, 6(5), 400-403.

Xu, J., Fan, D., Zhang, D., Guo, X., Zhou, W., and Dera, P.K. (2020) Phase Transition of Enstatite-Ferrosilite Solid Solutions at High Pressure and High Temperature: Constraints on Metastable Orthopyroxene in Cold Subduction. Geophysical Research Letters, 47(12), e2020GL087363.

Xu, J., Fan, D., Zhang, D., Ma, M., Zhou, Y., Tkachev, S.N., Zhou, W., and Dera, P.K. (2022) Phase Transitions of Fe-, Al- and Ca-Bearing Orthopyroxenes at High Pressure and High Temperature: Implications for Metastable Orthopyroxenes in Stagnant Slabs. Journal of Geophysical Research: Solid Earth, 127(1), e2021JB023133.

Xu, J., Zhang, D., Dera, P., Zhang, B., and Fan, D. (2017a) Experimental evidence for the survival of augite to transition zone depths, and implications for subduction zone dynamics. American Mineralogist, 102(7), 1516-1524.

Xu, J., Zhang, D., Fan, D., Dera, P.K., Shi, F., and Zhou, W. (2019) Thermoelastic Properties of Eclogitic Garnets and Omphacites: Implications for Deep Subduction of Oceanic Crust and Density Anomalies in the Upper Mantle. Geophysical Research Letters, 46(1), 179-188.

Xu, J., Zhang, D., Fan, D., Downs, R.T., Hu, Y., and Dera, P. (2017b) Isosymmetric pressure-induced bonding increase changes compression behavior of clinopyroxenes across jadeite-aegirine solid solution in subduction zones. Journal of Geophysical Research: Solid Earth, 122(1), 142-157.

Xu, J., Zhang, D., Fan, D., Zhang, J.S., Hu, Y., Guo, X., Dera, P., and Zhou, W. (2018) Phase Transitions in Orthoenstatite and Subduction Zone Dynamics: Effects of Water and Transition Metal Ions. Journal of Geophysical Research: Solid Earth, 123(4), 2723-2737.

Zhang, D., Dera, P.K., Eng, P.J., Stubbs, J.E., Zhang, J.S., Prakapenka, V.B., and Rivers, M.L. (2017) High Pressure Single Crystal Diffraction at PX^2. Journal of visualized experiments: JoVE(119), e54660.

Zhang, D., Hu, Y., and Dera, P.K. (2016) Compressional behavior of omphacite to 47 GPa. Physics and Chemistry of Minerals, 43(10), 707–715.

Zhang, D., Jackson, J.M., Chen, B., Sturhahn, W., Zhao, J., Yan, J., and Caracas, R. (2013a) Elasticity and lattice dynamics of enstatite at high pressure. Journal of Geophysical Research: Solid Earth, 118(8), 4071-4082.

Zhang, J.S., Dera, P., and Bass, J.D. (2012) A new high-pressure phase transition in natural Fe-bearing orthoenstatite. American Mineralogist, 97(7), 1070-1074.

Zhang, J.S., Reynard, B., Montagnac, G., and Bass, J.D. (2014) Pressure-induced *Pbca*–$P2_1/c$ phase transition of natural orthoenstatite: The effect of high temperature and its geophysical implications. Physics of the Earth and Planetary Interiors, 228, 150-159.

Zhang, J.S., Reynard, B., Montagnac, G., Wang, R.C., and Bass, J.D. (2013b) Pressure-induced *Pbca*-$P2_1/c$ phase transition of natural orthoenstatite: Compositional effect and its geophysical implications. American Mineralogist, 98(5-6), 986-992.

Zhang, L., Stanek, J., Hafner, S., Ahsbahs, H., Grünsteudel, H., and Metge, J. (1999) ^{57}Fe nuclear forward scattering of synchrotron radiation in hedenbergite $CaFeSi_2O_6$ at hydrostatic pressures up to 68 GPa. American Mineralogist, 84(3), 447-453.

Figure captions

Figure 1. Left: a representative diffraction image of Ni-, Fe-bearing orthopyroxene at 11.5 GPa, and the insert figure is a representative sample photo taken at 0.7 GPa. The rectangular area shows the zoomed-in region on the Right: zoomed-in diffraction images of the rectangular area on the left, which show diffraction peaks of opx in different phases. (a) α-opx at 11.5 GPa; (b) β-opx at 12.7 GPa; (c) γ-opx at 16.2 GPa; (d) α-popx at 33.8 GPa.

Figure 2. Unit-cell parameters and volume (a-e) of Ni-$En_{31}Fs_{65}$ as a function of pressure in comparison with En_{100} (Hugh-Jones and Angel 1994; Periotto et al. 2012; Xu et al. 2018) and Fs_{100} (Hugh-Jones et al. 1997; Xu et al. 2020); (f) Normalized unit-cell parameters of the Ni-$En_{31}Fs_{65}$ as a function of pressure and the shaded areas indicate the regions of the α-opx, β-opx, γ-opx, and β-popx. The red dashed lines shown in (a-e) are for guidance only, while the red solid lines shown in (e) indicate the EoS fit for α-opx and γ-opx.

Figure 3. M-O bond lengths in the MO_6 octahedra as a function of pressure. (a), (b), (c), and (d) show the data in the region of the α-opx, β-opx, γ-opx and β-popx, respectively.

Figure 4. Si-O bond lengths as a function of pressure. (a), (b), (c), and (d) show the data in the region of the α-opx, β-opx, γ-opx and β-popx, respectively.

Figure 5. MO_6 (a) and $SiO_{x\ (x = 4 \text{ or } 5 \text{ or } 6)}$ (b) polyhedral volumes of Ni-$En_{31}Fs_{65}$ as a function of pressure. The shaded areas indicate the metastable regions of the α-opx, β-opx, γ-opx, and β-popx.

Figure 6. Distortion index (a), quadratic elongation (b), and bond angle variance (c) of the MO_6 octahedra of Ni-$En_{31}Fs_{65}$ as a function of pressure. The shaded areas indicate the stable regions of the α-opx, β-opx, γ-opx and β-popx.

Figure 7. Distortion index (a), quadratic elongation (b), and bond angle variance (c) of the $SiO_{x\ (x = 4 \text{ or } 5 \text{ or } 6)}$ polyhedral volume of Ni-$En_{31}Fs_{65}$ as a function of pressure. The shaded areas indicate the regions of the α-opx, β-opx, γ-opx and β-popx.

Figure 8. Pressure-induced phase transitions of orthopyroxene as a function of M_{En} (molar percentage of enstatite in the solid solution orthopyroxene). The shaded areas indicate the phase regions for the En-Fs solid solution (adapted from Figure 2 in Xu et al. (2022)). The dashed lines represent weighted regressions of the data (P-M_{En}, Table S8) for the phase transitions and the regression equation of each dashed line is shown nearby. Note that $P_{tr} = 13.4(5) - 0.011(6)M_{En}$, $R^2 = 0.43$ is the formula adopted from Xu et al. (2022). The solid symbols represent the data of Ni-$En_{31}Fs_{65}$ obtained in this study.

Figure 9. Phase transition pressure of the pyroxene → post-pyroxene for orthopyroxene (En = enstatite) and clinopyroxene (Aeg = aegirine; Di = diopside; Cen = clinoenstatite; Cfs = clinoferrosilite). The insert figure at the bottom left shows a layer of typical chains formed by SiO_4 tetrahedra in orthopyroxene while that at the top right shows a layer of SiO_6 octahedra in post-pyroxene.

Figure 1

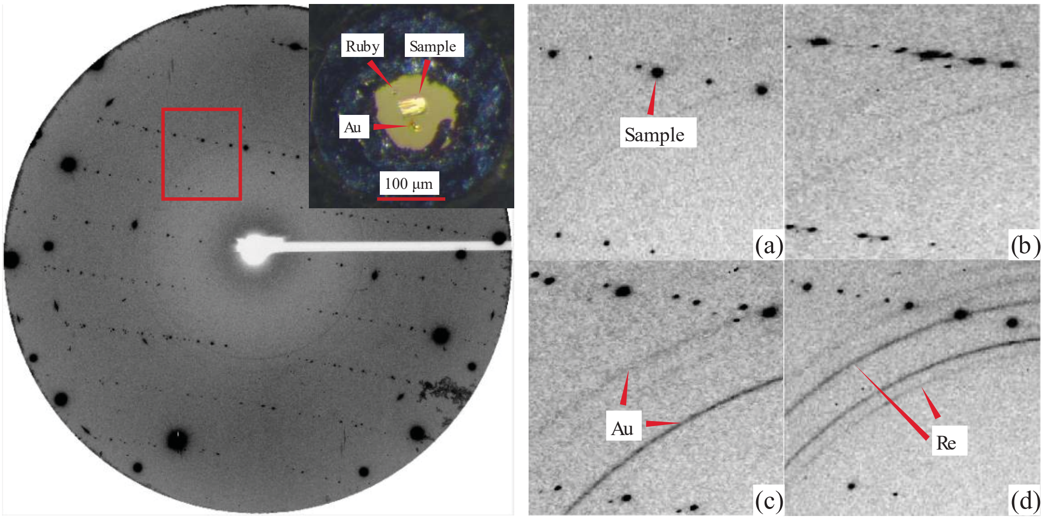

Figure 2

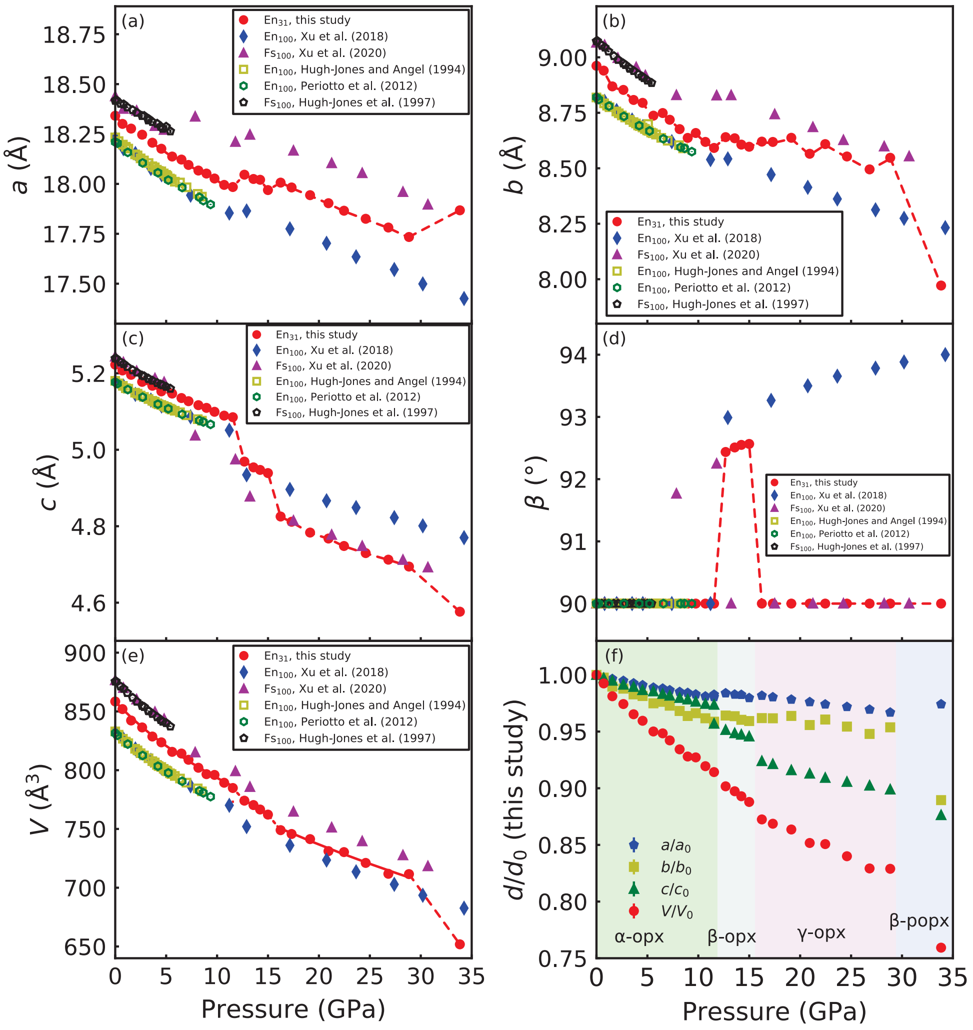
(a)
a (Å)
18.75
18.50
18.25
18.00
17.75
17.50
En_{31}, this study
En_{100}, Xu et al. (2018)
Fs_{100}, Xu et al. (2020)
En_{100}, Hugh-Jones and Angel (1994)
En_{100}, Periotto et al. (2012)
Fs_{100}, Hugh-Jones et al. (1997)
(b)
b (Å)
9.00
8.75
8.50
8.25
8.00
(c)
c (Å)
5.2
5.0
4.8
4.6
(d)
β (°)
94
93
92
91
90
(e)
V (Å^3)
900
850
800
750
700
650
(f)
d/d_0 (this study)
1.00
0.95
0.90
0.85
0.80
0.75
a/a_0
b/b_0
c/c_0
V/V_0
α-opx
β-opx
γ-opx
β-popx
0
5
10
15
20
25
30
35
Pressure (GPa)

Figure 3

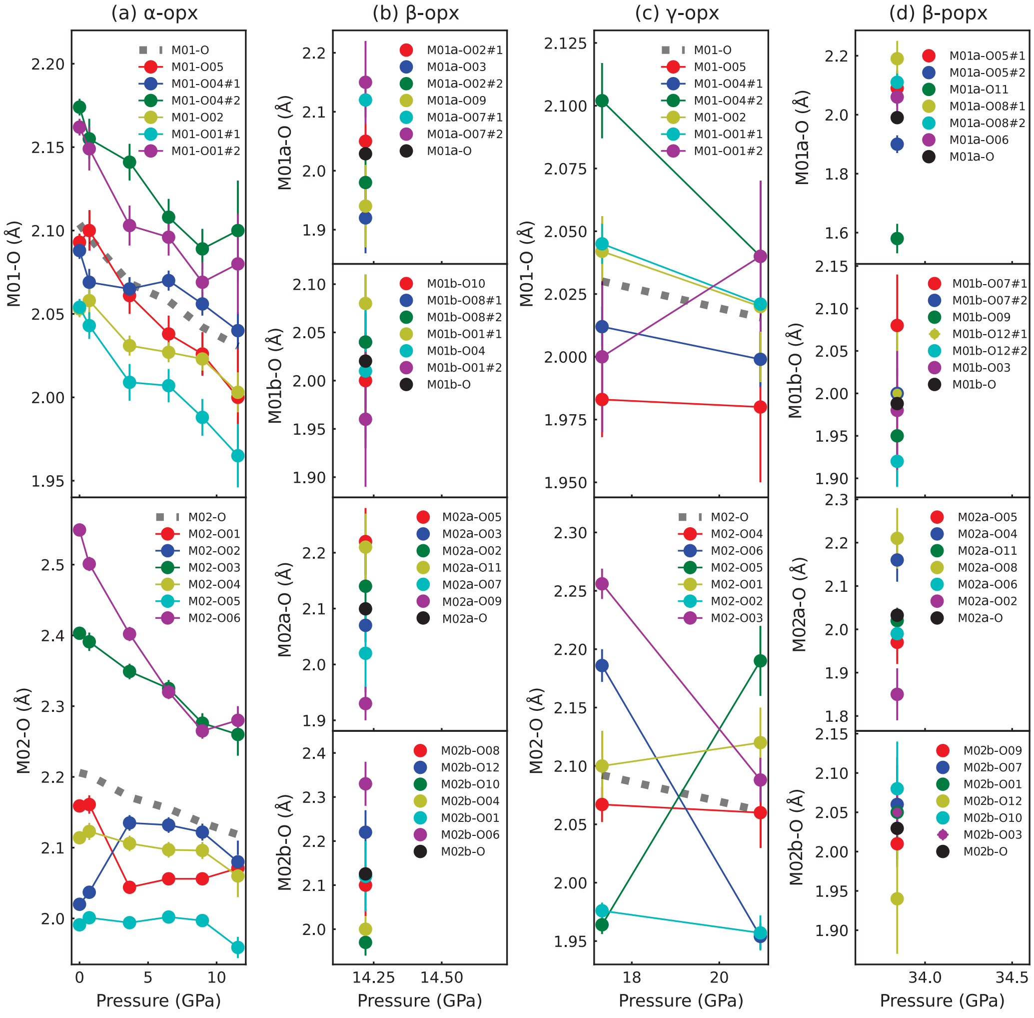
(a) α-opx
(b) β-opx
(c) γ-opx
(d) β-popx
M01-O (Å)
M02-O (Å)
M01a-O (Å)
M01b-O (Å)
M02a-O (Å)
M02b-O (Å)
Pressure (GPa)
M01-O
M01-O05
M01-O04#1
M01-O04#2
M01-O02
M01-O01#1
M01-O01#2
M02-O
M02-O01
M02-O02
M02-O03
M02-O04
M02-O05
M02-O06
M01a-O02#1
M01a-O03
M01a-O02#2
M01a-O09
M01a-O07#1
M01a-O07#2
M01a-O
M01b-O10
M01b-O08#1
M01b-O08#2
M01b-O01#1
M01b-O04
M01b-O01#2
M01b-O
M02a-O05
M02a-O03
M02a-O02
M02a-O11
M02a-O07
M02a-O09
M02a-O
M02b-O08
M02b-O12
M02b-O10
M02b-O04
M02b-O01
M02b-O06
M02b-O
M02-O04
M02-O06
M02-O05
M02-O01
M02-O02
M02-O03
M01a-O05#1
M01a-O05#2
M01a-O11
M01a-O08#1
M01a-O08#2
M01a-O06
M01b-O07#1
M01b-O07#2
M01b-O09
M01b-O12#1
M01b-O12#2
M01b-O03
M02a-O04
M02a-O08
M02a-O06
M02b-O09
M02b-O07
M02b-O03
0
5
10
14.25
14.50
18
20
34.0
34.5

Figure 4

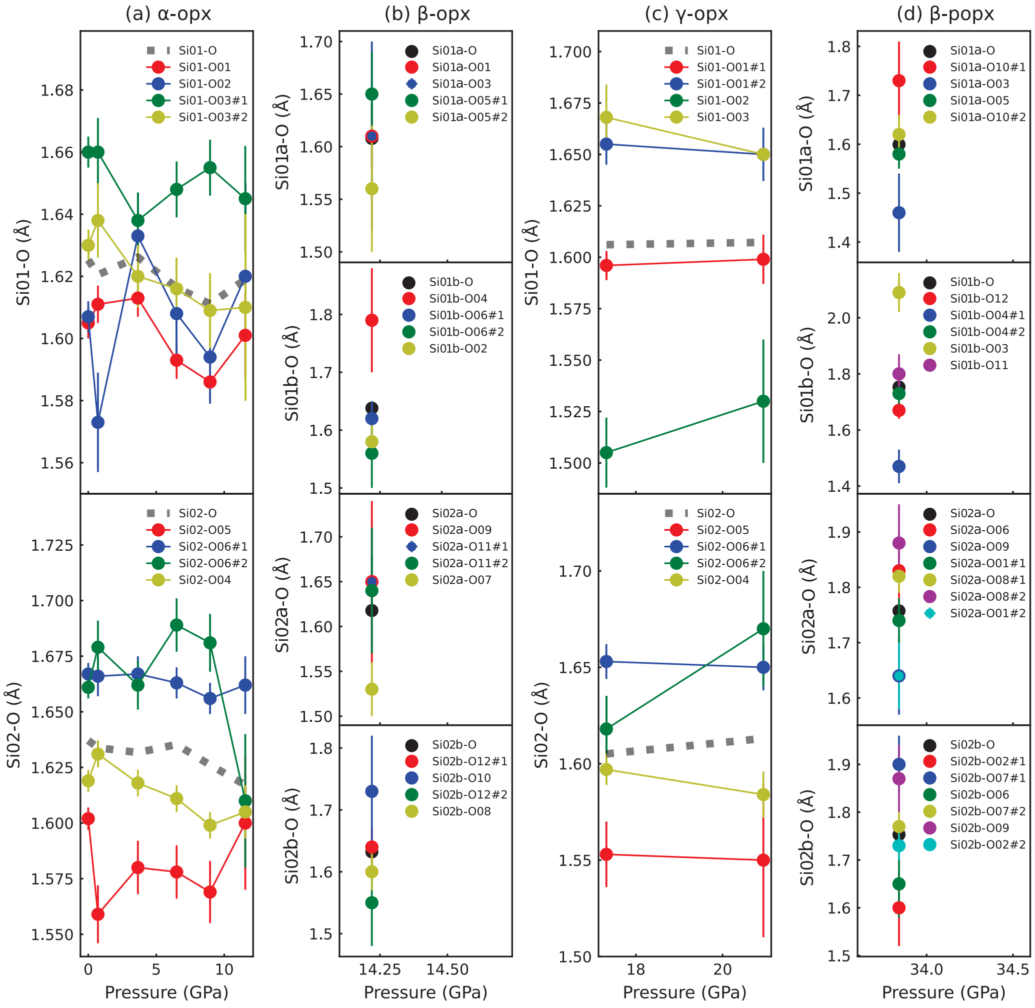
(a) α-opx
(b) β-opx
(c) γ-opx
(d) β-popx
Si01-O (Å)
Si02-O (Å)
Si01a-O (Å)
Si01b-O (Å)
Si02a-O (Å)
Si02b-O (Å)
Pressure (GPa)
Si01-O
Si01-O01
Si01-O02
Si01-O03#1
Si01-O03#2
Si02-O
Si02-O05
Si02-O06#1
Si02-O06#2
Si02-O04
Si01a-O
Si01a-O01
Si01a-O03
Si01a-O05#1
Si01a-O05#2
Si01b-O
Si01b-O04
Si01b-O06#1
Si01b-O06#2
Si01b-O02
Si02a-O
Si02a-O09
Si02a-O11#1
Si02a-O11#2
Si02a-O07
Si02b-O
Si02b-O12#1
Si02b-O10
Si02b-O12#2
Si02b-O08
Si01-O
Si01-O01#1
Si01-O01#2
Si01-O02
Si01-O03
Si02-O
Si02-O05
Si02-O06#1
Si02-O06#2
Si02-O04
Si01a-O
Si01a-O10#1
Si01a-O03
Si01a-O05
Si01a-O10#2
Si01b-O
Si01b-O12
Si01b-O04#1
Si01b-O04#2
Si01b-O03
Si01b-O11
Si02a-O
Si02a-O06
Si02a-O09
Si02a-O01#1
Si02a-O08#1
Si02a-O08#2
Si02a-O01#2
Si02b-O
Si02b-O02#1
Si02b-O07#1
Si02b-O06
Si02b-O07#2
Si02b-O09
Si02b-O02#2
1.68
1.66
1.64
1.62
1.60
1.58
1.56
1.725
1.700
1.675
1.650
1.625
1.600
1.575
1.550
0
5
10
1.70
1.65
1.60
1.55
1.50
1.8
1.7
1.6
1.5
1.70
1.65
1.60
1.55
1.50
1.8
1.7
1.6
1.5
14.25
14.50
1.700
1.675
1.650
1.625
1.600
1.575
1.550
1.525
1.500
1.70
1.65
1.60
1.55
1.50
18
20
1.8
1.7
1.6
1.5
1.4
2.0
1.8
1.6
1.4
1.9
1.8
1.7
1.6
1.9
1.8
1.7
1.6
1.5
34.0
34.5

Figure 5

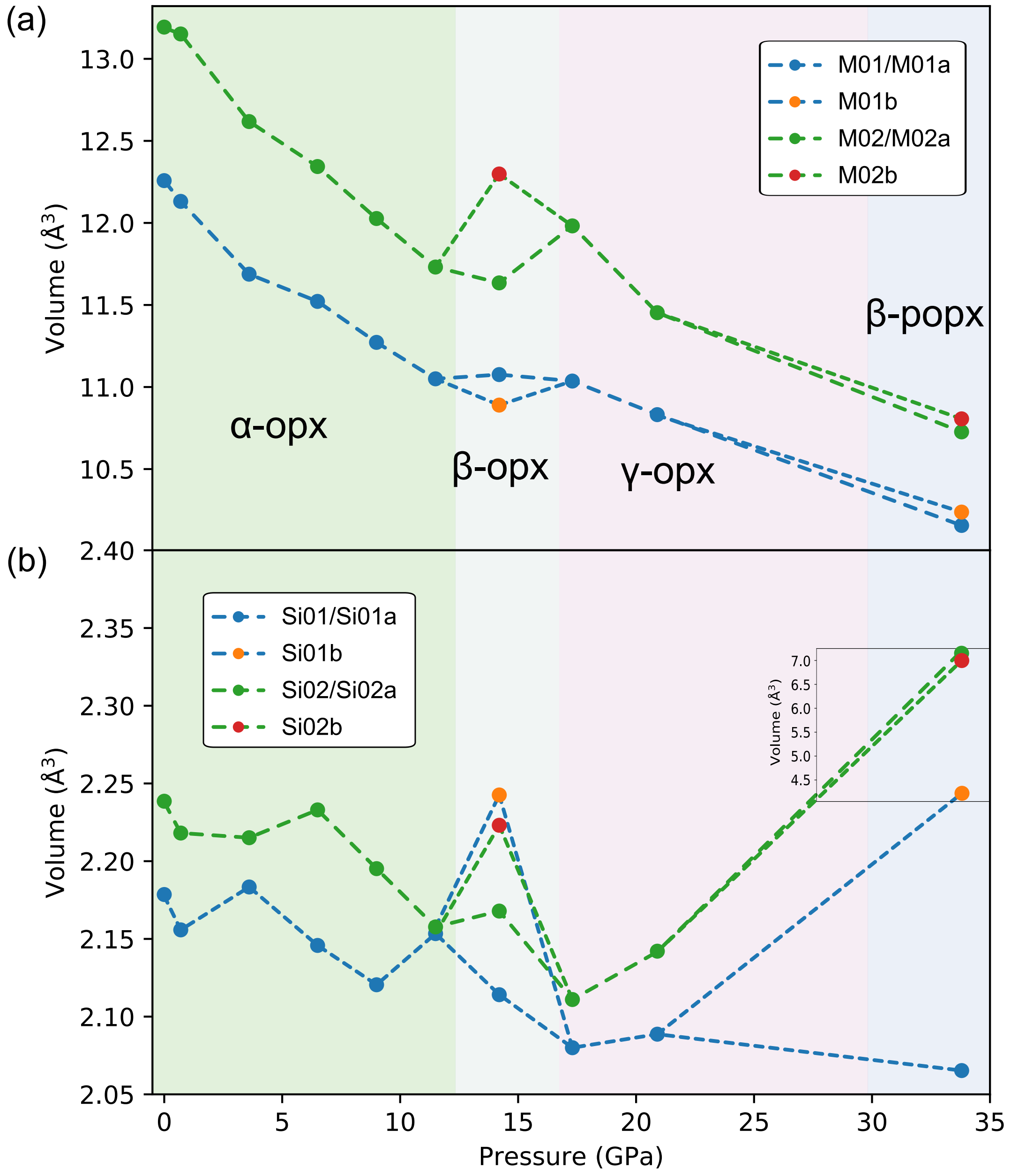
(a)
13.0
12.5
12.0
11.5
11.0
10.5
Volume (Å³)
M01/M01a
M01b
M02/M02a
M02b
α-opx
β-opx
γ-opx
β-popx
(b)
2.40
2.35
2.30
2.25
2.20
2.15
2.10
2.05
Volume (Å³)
Si01/Si01a
Si01b
Si02/Si02a
Si02b
7.0
6.5
6.0
5.5
5.0
4.5
Volume (Å³)
0
5
10
15
20
25
30
35
Pressure (GPa)

Figure 6

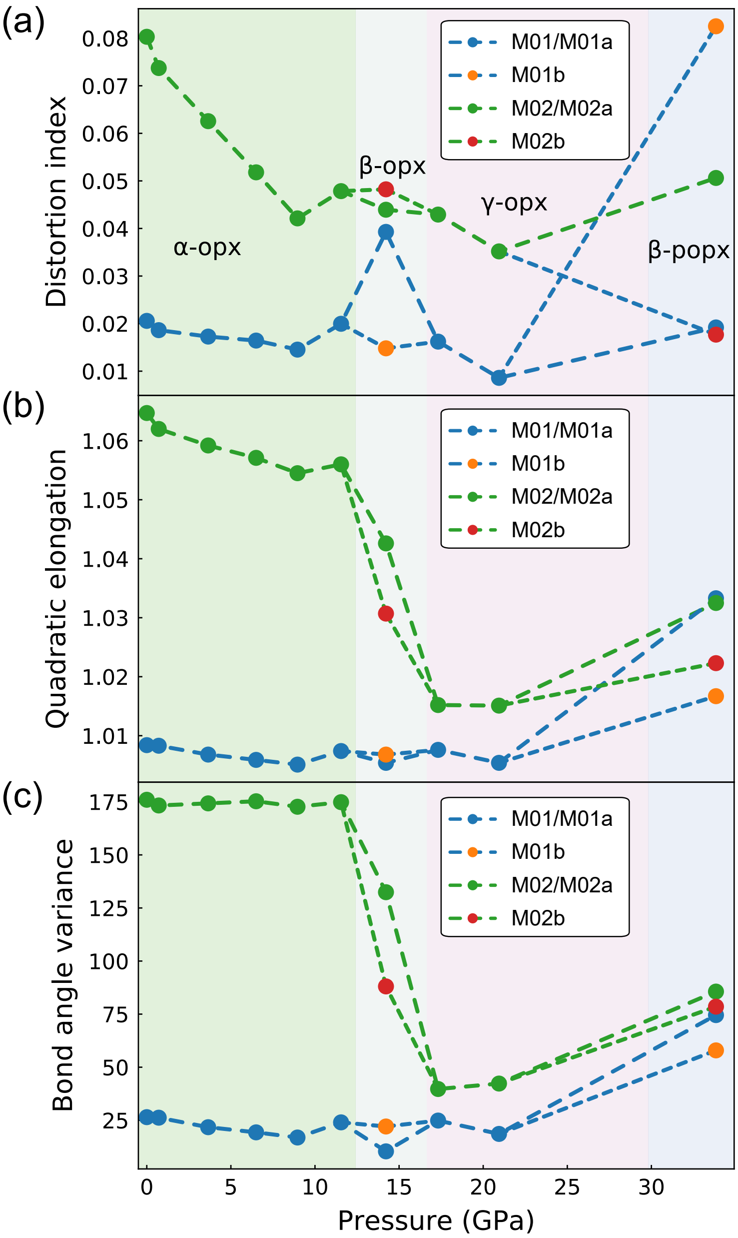
(a)
Distortion index
0.08
0.07
0.06
0.05
0.04
0.03
0.02
0.01
α-opx
β-opx
γ-opx
β-popx
M01/M01a
M01b
M02/M02a
M02b
(b)
Quadratic elongation
1.06
1.05
1.04
1.03
1.02
1.01
M01/M01a
M01b
M02/M02a
M02b
(c)
Bond angle variance
175
150
125
100
75
50
25
M01/M01a
M01b
M02/M02a
M02b
0
5
10
15
20
25
30
Pressure (GPa)

Figure 7

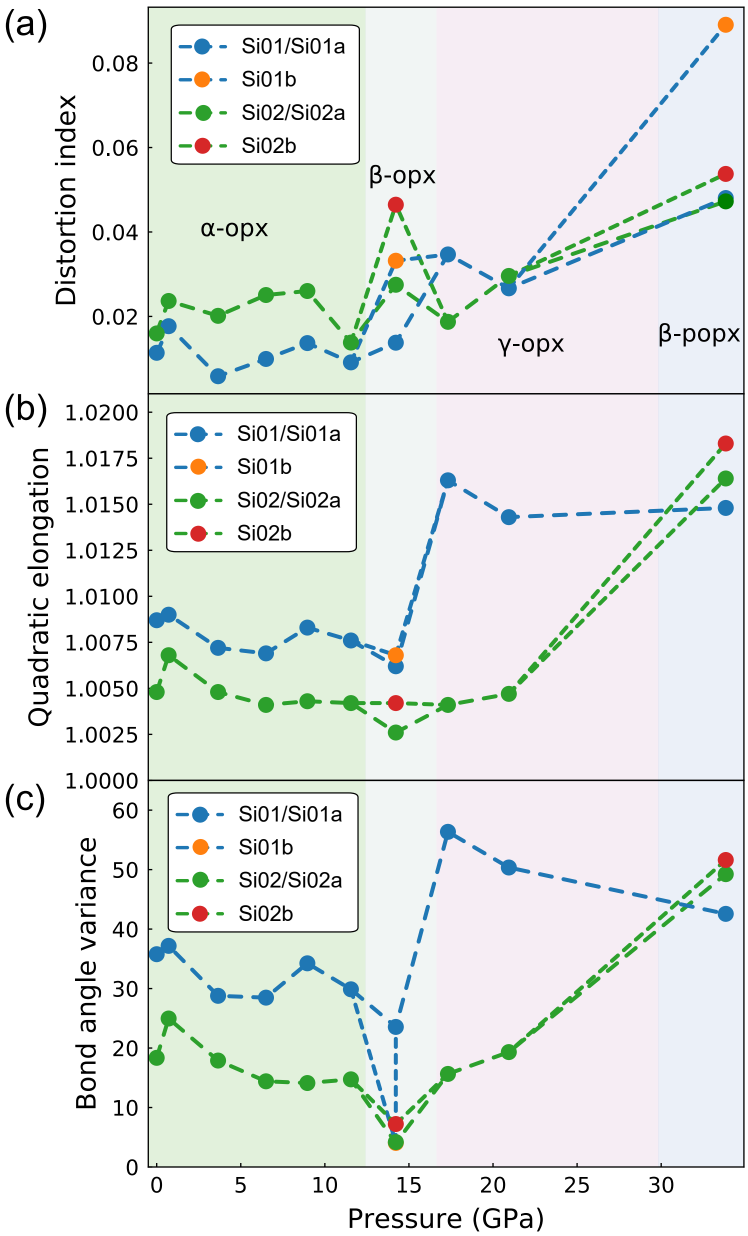
(a)
Si01/Si01a
Si01b
Si02/Si02a
Si02b
Distortion index
0.02
0.04
0.06
0.08
α-opx
β-opx
γ-opx
β-popx
(b)
Quadratic elongation
1.0000
1.0025
1.0050
1.0075
1.0100
1.0125
1.0150
1.0175
1.0200
(c)
Bond angle variance
0
10
20
30
40
50
60
0
5
10
15
20
25
30
Pressure (GPa)

Figure 8

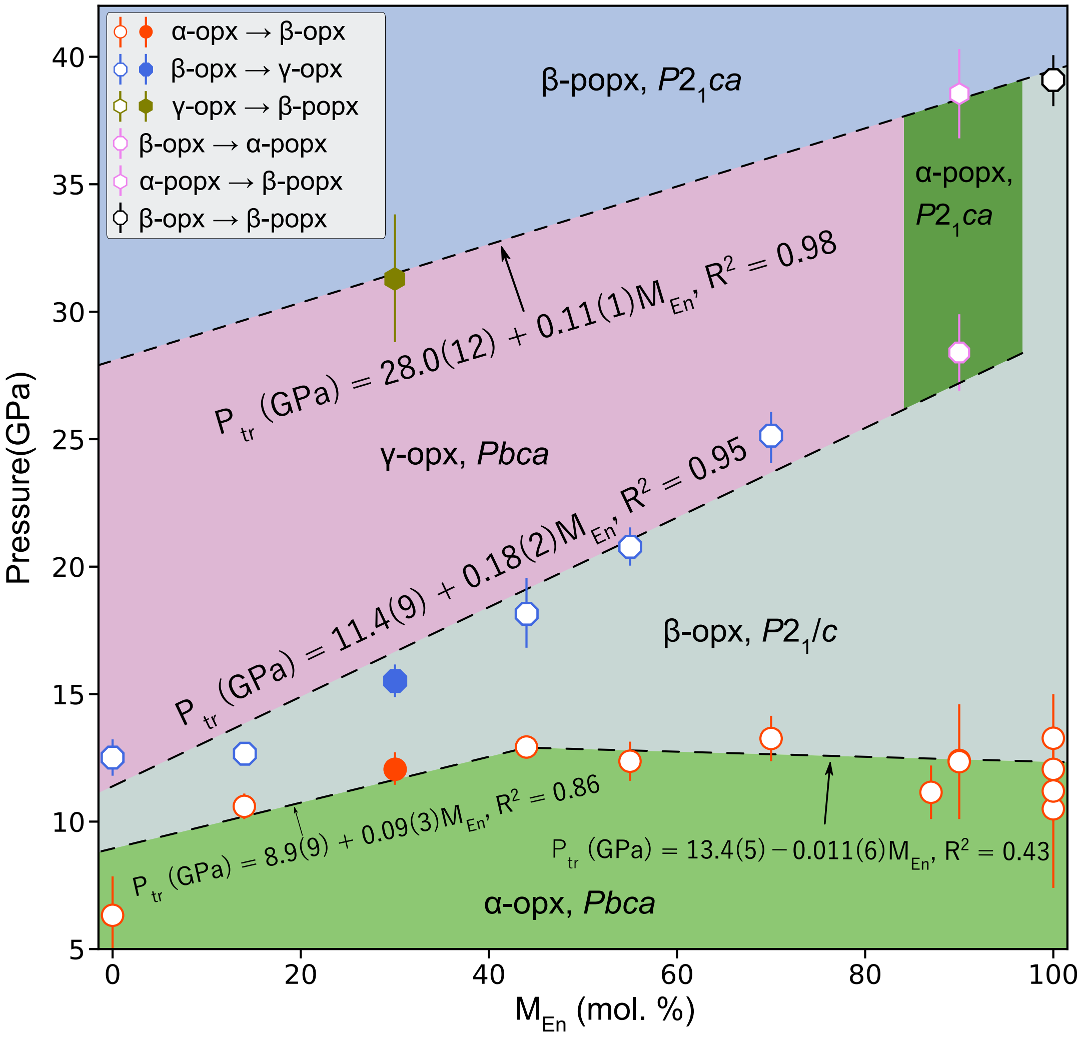
α-opx → β-opx
β-opx → γ-opx
γ-opx → β-popx
β-opx → α-popx
α-popx → β-popx
β-opx → β-popx
β-popx, $P2_1ca$
α-popx, $P2_1ca$
P_{tr} (GPa) = 28.0(12) + 0.11(1)M_{En}, R^2 = 0.98
γ-opx, *Pbca*
P_{tr} (GPa) = 11.4(9) + 0.18(2)M_{En}, R^2 = 0.95
β-opx, $P2_1/c$
P_{tr} (GPa) = 8.9(9) + 0.09(3)M_{En}, R^2 = 0.86
P_{tr} (GPa) = 13.4(5) − 0.011(6)M_{En}, R^2 = 0.43
α-opx, *Pbca*
Pressure(GPa)
5
10
15
20
25
30
35
40
0
20
40
60
80
100
M_{En} (mol. %)

Figure 9

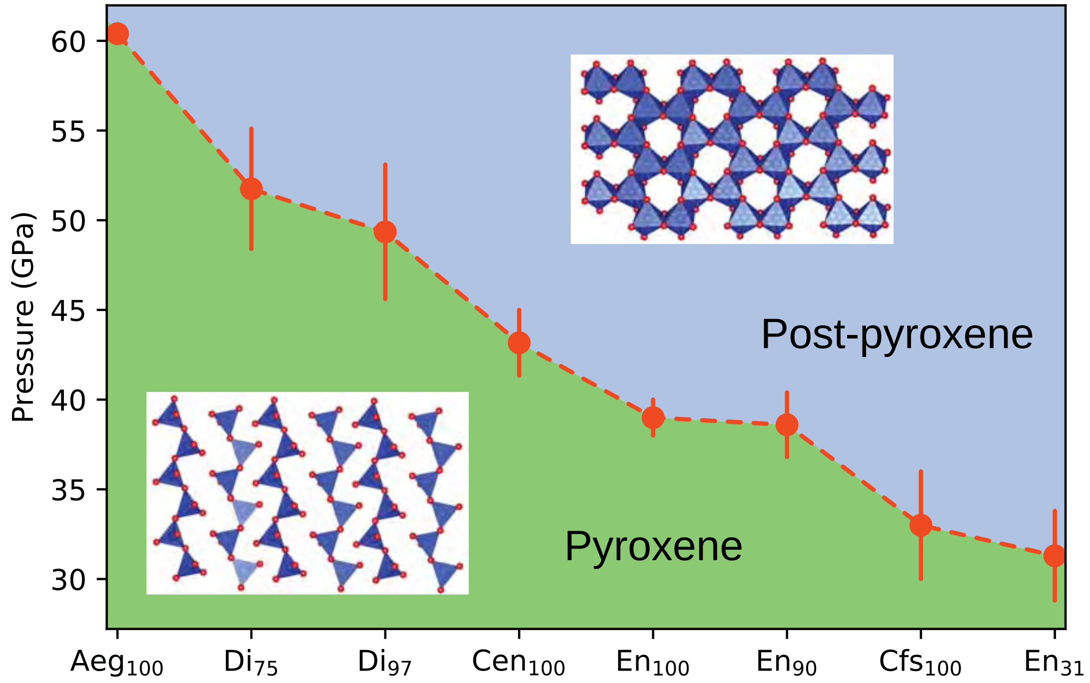
60
55
50
45
40
35
30
Pressure (GPa)
Post-pyroxene
Pyroxene
Aeg$_{100}$
Di$_{75}$
Di$_{97}$
Cen$_{100}$
En$_{100}$
En$_{90}$
Cfs$_{100}$
En$_{31}$